MATERIALS SCIENCE

Ultrastrong lightweight compositionally complex steels via dual-nanoprecipitation

Zhangwei Wang[1]*, Wenjun Lu[1]*, Huan Zhao[1], Christian H. Liebscher[1], Junyang He[1], Dirk Ponge[1], Dierk Raabe[1], Zhiming Li[2,3]*

High-performance lightweight materials are urgently needed, given the pressing quest for weight reduction and the associated energy savings and emission reduction. Here, by incorporating the multi–principal element feature of compositionally complex alloys, we develop the concept of lightweight steels further and propose a new class of compositionally complex steels (CCSs). This approach allows us to use the high solid solution strengthening and shift the alloys' compositions into previously unattainable phase regions where both nanosized shearable κ-carbides and non-shearable B2 particles are simultaneously formed. The achievement of dual-nanoprecipitation in our CCSs leads to materials with ultrahigh specific tensile strength (up to 260 MPa·cm^3 g^{-1}) and excellent tensile elongation (13 to 38%), a combination outperforming all other high-strength high-entropy alloys and advanced lightweight steels. Our concept of CCSs is thus useful for guiding the design of ultrastrong lightweight metallic materials.

INTRODUCTION

The design of steels with high strength, toughness, and ductility combined with low mass density is an important task for saving energy and reducing emissions at maintained safety levels in multiple transportation applications. For example, reducing a vehicle's weight translates linearly to a corresponding reduction in fuel consumption, with a rule of thumb value of 0.5 liters less fuel per 100 kg of weight reduction. Although other lightweight materials, e.g., Al-alloys, Mg-alloys, and carbon fiber composites, are available or under development, the unique combination of absolute strength, specific strength, ductility, toughness, and cost-effectiveness makes advanced lightweight Fe-based steels particularly attractive for future key engineering applications (*1*). In this context, the Fe-Mn-Al-C system has gained much attention since the addition of Al into the Fe-Mn-C system is effective to achieve both up to ~10% weight reduction and improved strength and ductility compared to conventional steels (*2*, *3*). More specifically, Fe-Mn-Al-C steels with austenitic [face-centered cubic (FCC)] solid solution matrix and nanosized L'1$_2$ (ordered FCC) κ-carbides reach a tensile strength of ~1190 MPa (specific tensile strength of 183 MPa·cm^3 g^{-1}) at an elongation of ~30% under tensile loading (*4*).

However, the shearing of the coherent κ-carbides at high stresses leads to local strain softening, which can cause strain localization (*5*). Also, at grain boundaries, the κ-carbides become incoherent, promoting crack initiation, which leads to embrittlement, particularly at high Al and C contents (*2*). Thus, for further enhancing the mechanical properties, non-shearable incoherent B2 (ordered body-centered cubic) particles, instead of κ-carbides, have been introduced into Fe-Mn-Al-C–based austenitic steels (*6*). The uniformly distributed hard B2 particles enable pronounced local strain hardening, since the dislocations must bow out and bypass them, leaving additional dislocation loops around the particles behind, an effect referred to as Orowan strengthening. This mechanism leads to very high specific strength values of up to 233 MPa·cm^3 g^{-1} for an alloy [referred to as high–specific strength steels (HSSSs)] with 22 vol. % of B2 precipitates (*6*, *7*). Higher strength values require larger volume fractions of B2 particles, yet only at a significant expense of ductility, due to the intrinsically brittle nature of the B2 intermetallic compound (*6*, *8*).

Because of these limitations of the existing alloy design concepts, we introduce here a new approach in which we strengthen a low-density solid solution matrix simultaneously by a dual-nanoprecipitation system containing both κ-carbides and B2 particles. Since the conventional thermodynamic working point is not accessible to realize this dual-precipitation strategy, we designed a low-density (6.6 g/cm^3) steel-type alloy, which uses merits of the recently introduced multi–principal element approach referred to as compositionally complex alloys (CCAs) or high-entropy alloys (HEAs) (*9*–*11*). More specifically, we propose here a new class of compositionally complex steels (CCSs) consisting of five principal elements including C in nonequiatomic ratios with Fe holding the highest atomic fraction [48 atomic % (at. %)], and each element has an atomic fraction of no less than 5 at. %. This novel concept not only exploits the massive solid solution strengthening provided by the multiple principal elements in the matrix but also enables tuning the composition into phase regions where both nanosized shearable κ-carbides and non-shearable B2 particles exist.

RESULTS AND DISCUSSION

Developing CCSs

We realize the novel concept of the CCSs with dual-nanoprecipitation here in a model material with a composition of Fe-26Mn-16Al-5Ni-5C (at. %). Such CCS consists of five major elements where the content of each element is around or above 5 at. %. It is worth noting that C, which is an interstitial element in this material, can unexpectedly reach a very high solid solution concentration level otherwise only accessible for substitutional elements. A large amount of Mn is added to stabilize the austenite matrix (*12*). Al and C reduce the mass density and promote the formation of L'1$_2$ κ-carbides (*13*). The addition of Ni induces the formation of NiAl-type B2 particles (*14*).

[1]Max-Planck-Institut für Eisenforschung, Max-Planck-Str. 1, 40237 Düsseldorf, Germany. [2]School of Materials Science and Engineering, Central South University, 410083 Changsha, China. [3]State Key Laboratory of Powder Metallurgy, Central South University, 410083 Changsha, China.
*Corresponding author. Email: zh.wang@mpie.de (Z.W.); w.lu@mpie.de (W.L.); lizhiming@csu.edu.cn (Z.L.)

The concept thus unifies, so far, less related approaches from steels, HEAs, and nanoprecipitation systems via using low-cost ingredients. The latter aspect is essential since the expensive alloying elements typically used in HEAs have impeded their engineering applications (see fig. S1).

The CCSs were produced in line with widely applied procedures in industries. The as-cast materials were first homogenized at 1200°C and then hot-rolled at 1100°C to strips with a thickness of 2.5 mm, followed by cold-rolling to 60% reduction in thickness and annealing for 3 min at 800°, 850°, and 900°C, respectively (see Materials and Methods).

Unique dual-nanoprecipitation

Figure 1 shows the typical microstructure of the model CCS annealed at 800°C. Electron backscatter diffraction (EBSD) inverse pole figure (Fig. 1A) and phase maps (Fig. 1B) reveal B2 particles in the partially recrystallized austenitic matrix. The FCC matrix and B2 particles are also observed by x-ray diffraction (XRD) results (see fig. S2D). These fine B2 particles (~1 vol. %), with a size range from several hundred nanometers to 1 μm, were formed during hot-rolling. The partially recrystallized austenite has a bimodal microstructure, i.e., non-recrystallized large grains with an average size of 15 μm and an area fraction of ~92% plus recrystallized fine grains with an average size of ~350 nm occupying an area fraction of ~8% (see fig. S2). The backscattered electron (BSE) image in Fig. 1C shows that the second type of precipitates with darker contrast is present in the CCS in addition to the B2 particles, which appear in light contrast.

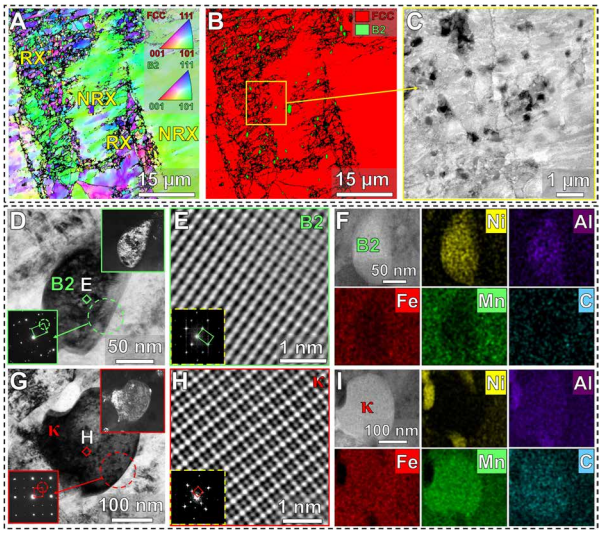

Fig. 1. Microstructures of the CCS annealed at 800°C. (**A**) EBSD IPF map. (**B**) EBSD phase map. (**C**) BSE image. The BSE image shows the microstructure of the marked region in the phase map, indicating the formation of a dual-nanoprecipitation system: one with lighter contrast and the other one with darker contrast. The IPF map reveals recrystallized (RX) and non-recrystallized (NRX) regions. (**D** to **F**) BF TEM image, HR HAADF-STEM image, and EDS maps of the B2 phase, respectively. (**G** to **I**) BF TEM image, HR HAADF-STEM image, and EDS maps of the κ-carbide, respectively. SAED patterns [insets in (D) and (G)] indicate the crystal structures of B2 and κ-carbide. DF TEM images taken from the superlattice reflections are shown [insets in (D) and (G)]. FFT patterns [insets in (E) and (H)] confirm the ordered structures of B2 and κ-carbide. The indexes of SAED patterns are shown in the Supplementary Materials and fig. S2. IPF, BSE, SAED, FFT, and EDS refer to the inverse pole figure, backscattered electron, selected area electron diffraction pattern, fast Fourier transform, and energy dispersive X-ray spectroscopy, respectively.

We determined the crystal structures and chemical compositions of the two types of precipitates by transmission electron microscopy (TEM) and energy-dispersive x-ray spectroscopy (EDS) analysis. The selected area electron diffraction (SAED) pattern (inset in Fig. 1D) taken along the ⟨110⟩ zone axis confirms a B2 structure. The morphology of the B2 particle is revealed by both bright-field (BF) (Fig. 1D) and dark-field (DF) TEM imaging (inset in Fig. 1D) taken from the {001} superlattice reflection. According to the EDS maps in Fig. 1F, the B2 precipitate is rich in Ni and Al but depleted in Fe, Mn, and C, indicating a NiAl-type B2 phase (*15*). Figure 1G shows the BF TEM image of the second precipitate type. The corresponding SAED pattern (inset in Fig. 1G) shows an ordered FCC structure of this precipitate, as revealed by the {100} superlattice reflection along the ⟨001⟩ zone axis. The EDS maps in Fig. 1I show that the composition of this ordered precipitate is close to that of the austenite matrix, yet with a slightly higher content of C and much lower content of Ni, suggesting an $(Fe, Mn)_3AlC$-type κ-carbide (*16*). The periodicity in atomic intensity mapped by the high-resolution (HR) high-angle annular dark-field (HAADF) scanning TEM (STEM) images, which arises from the difference in Z-contrast among the neighboring atomic columns, indicates the regular occupation of Al atoms both in the ordered B2 particles (Fig. 1E) and in the ordered κ-carbides (Fig. 1H). We also observed coprecipitation of nano-sized B2 and κ-carbides where three B2 particles form adjacent to a κ-carbide, as shown by the HAADF-STEM image and EDS maps in Fig. 1I. These results document the successful dual-nanoprecipitation of B2 and κ-carbide in the CCS, an approach not realized before in materials design.

The HAADF-STEM analysis (see fig. S3) shows abundant nanoprecipitates uniformly distributed in the FCC matrix. The corresponding EDS maps identify some of them as B2 particles (NiAl-rich regions), whereas the detection of the κ-carbides is more challenging since their composition is close to that of the matrix (see Fig. 1I). We thus probed the coprecipitation of B2 and κ-carbide by using the Z-contrast in HR HAADF-STEM mode (Fig. 2A). Regions of austenitic matrix with embedded κ-carbides are revealed by the corresponding fast Fourier transform (FFT) patterns (Fig. 2, B and C). The diffuse interfaces between the two phases indicate interface coherency. Some regions in Fig. 2A are blurry and out of focus. These have been identified as (Ni, Al)-rich B2 regions in the corresponding EDS maps (Fig. 2D). These results suggest that the B2 phase is incoherent with the austenitic matrix.

We next performed atom probe tomography (APT) measurements for high-precision composition probing of two types of nanoprecipitates. Figure 2E shows a typical reconstructed APT dataset highlighted by the iso-composition surfaces of 30 at. % Ni, 30 at. % Al, and 10 at. % C, respectively. The B2 particles have elliptical shapes with sharp matrix/precipitate interfaces, whereas the irregular-shaped κ-carbides show blurred interfaces with the austenitic matrix (see movie S1). According to the combined TEM and APT analysis, the average sizes of these uniformly distributed B2 nanoparticles and κ-carbides are ~6 and ~4 nm, respectively (see figs. S3, C and D). The density maps of Ni and C reveal that the Ni-rich and C-rich regions are always in contact with each other (Fig. 2F), supporting the coprecipitation mechanism of B2 and κ-carbide (see movie S1 and fig. S3E). The elemental composition profiles of the matrix, B2, and κ-carbide obtained from the APT analysis are shown in Fig. 2G. The ratio of the Ni and Al contents

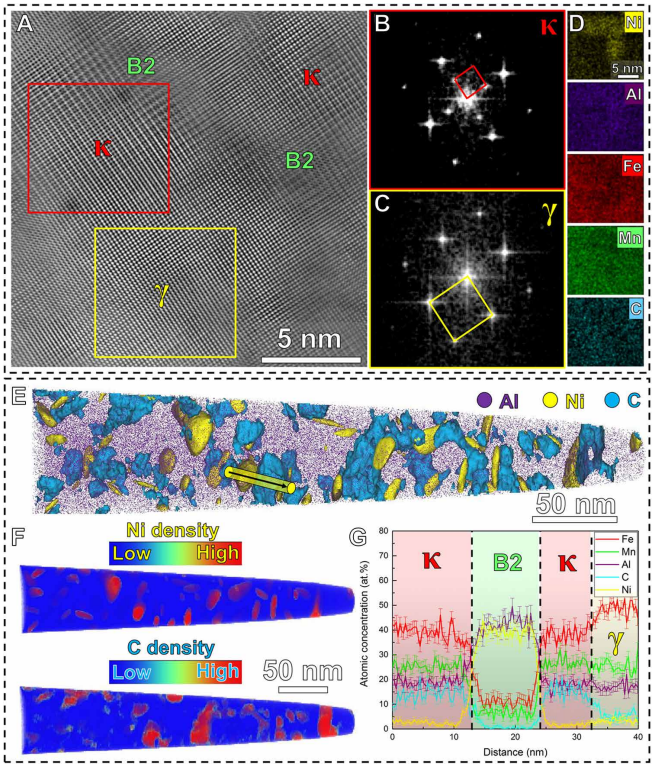

Fig. 2. Characterization of dual-nanoprecipitation of B2 and κ-carbide at atomic scales. (**A**) HR HAADF-STEM image showing the atomic structures of FCC austenitic (γ) matrix, B2 phase, and κ-carbide. (**B**) and (**C**) are FFT patterns confirming the structure of γ matrix and κ-carbide, respectively. (**D**) EDS maps of the same sample region in (A) indicate two regions belonging to the B2 phases. (**E**) APT results including atomic maps highlighted by iso-composition surfaces of 30 at. % Ni, 30 at. % Al, and 10 at. % C. (**F**) Atomic density maps of Ni and C. (**G**) One-dimensional compositional profiles showing the exact chemical compositions of γ matrix, κ-carbide, and B2 phase.

is close to 1 in the B2 phase, while the C content is nearly zero. By contrast, C is rich in κ-carbide, with a partitioning coefficient of ~3 between κ-carbide and matrix.

The dual-nanoprecipitation of B2 and κ-carbide distinguishes the CCSs from other lightweight materials. In the established Fe-Mn-Al-C lightweight alloys, ~2- to 10-nm-sized coherent κ-carbides form uniformly inside the austenitic grain interiors via spinodal decomposition (*2*, *17*, *18*). This mechanism occurs upon annealing at temperatures ranging from 450° to 650°C usually from 1 hour to several hours (*2*). Above ~720°C, κ-carbides cease to form in Fe-30Mn-9Al-1C (wt. %) lightweight steels (*19*). In contrast, in the current CCS, a high number density of κ-carbides is formed at a temperature as high as 800°C. The APT results (Fig. 2G) show that C has very little solubility in the B2 phase, while κ-carbides are enriched in C. This means that formation of any of these two types of precipitates creates a depleted or respectively enriched environment by partitioning in the adjacent matrix, which, in turn, drives the formation of the respectively other type of precipitate nearby. This effect promotes a very dense nanoscale coprecipitation backpack topology of κ-carbide and B2 in this material. Here, the backpack topology refers to the fact that the two types of nanoprecipitates are in contact with each other (*20*), as further revealed in fig. S3E. This feature prevails even after coarsening of the κ-carbides and B2 precipitates at higher temperatures, e.g., 900°C, demonstrating high stability of the dual-nanoprecipitation system (see fig. S4).

Outstanding mechanical properties

To evaluate the specific effects of this dual-nanoparticle precipitation strategy on the mechanical performance of the new CCSs, we conducted uniaxial tension tests. Representative engineering stress-strain curves are shown in Fig. 3A. The ultimate tensile strength (UTS) of the CCS annealed at 800°C for 3 min (CCS-1) is 1.7 GPa, and the corresponding specific UTS is 260 MPa·cm^3 g^{-1}. The specific UTS, together with 13% total elongation (uniform elongation of 11%), surpasses previously reported HSSS (*6*), dual-phase heterogeneous lamella structured HEAs (*21*), and conventional maraging steels (*22*), as shown in Fig. 3B. Further, our CCS shows comparable specific UTS to the recently developed advanced maraging steels (specific UTS of 287 MPa·cm^3 g^{-1}), yet with significantly improved ductility (tensile elongation of 13% versus 8%) (*23*). Depending on the specific application targeted, the mechanical response of the CCSs can also be tuned with other annealing conditions. For instance, a high tensile elongation of 38% can be achieved when increasing the annealing temperature to 900°C (CCS-3), along with a UTS of 1.4 GPa and a specific UTS of 222 MPa·cm^3 g^{-1}. Because of the higher annealing temperature, the CCS-3 shows a higher fraction of recrystallized material, larger grain size, and larger spacing among the precipitates compared to the CCS-1 (see Materials and Methods), which allows for less confined dislocation motion and thus causes a significant increase of the tensile elongation. The resulting combination of specific strength and ductility of the CCSs again exceeds that of all other bulk high-strength HEAs (*21*, *24*–*33*), lightweight steels (*4*, *6*, *7*, *34*–*36*), and maraging steels (*22*, *23*) (Fig. 3B).

By using low-angle annular dark-field (LAADF) STEM probing, we examined the material's deformation microstructure to uncover the strengthening mechanisms caused by the dual-nanoprecipitation of κ-carbides and B2 particles. Figure 4A shows dislocations (in bright contrast) at a strain of 1.5% of the model CCS annealed at 800°C. The zoom-in image in Fig. 4B reveals that the dislocations cut through the κ-carbide, whereas they are pinned by the B2 particles. In this case, the structure of the κ-carbide is determined using the FFT patterns (insets in Fig. 4B), and B2 is identified by the EDS maps in Fig. 4C. These deformation mechanisms prevail also at a higher strain of 7% (see fig. S5). Shearing of the dispersed κ-carbides requires a high stress (up to ~500 MPa in conventional weight-reduced steels) (*37*), and the hard B2 particles produce a strong strengthening effect as they enforce dislocation bypassing (*6*, *38*). This nanoscale interplay of the κ-carbide and B2 phase dual-nanoprecipitation system thus yields a significant strength contribution of ~1 GPa, explaining the high yield strength of the CCSs (strength calculations are shown in Materials and Methods). Given its high strength, the CCSs also have unusually good ductility. We explain this in terms of the nanoscale homogenization of the plastic flow and of the internal stress fields. The coherent interfaces between κ-carbide and the austenitic matrix disfavor crack nucleation due to the elastic compliance between the two phases (*23*, *32*). The pinning of dislocations by B2 particles results in local strain hardening, preventing dislocation localization, which could otherwise result from local strain softening caused by shearable coherent κ-carbides, an effect that can lead to strain localization and damage initiation in other alloys (*5*). In the current alloy, this localization effect is

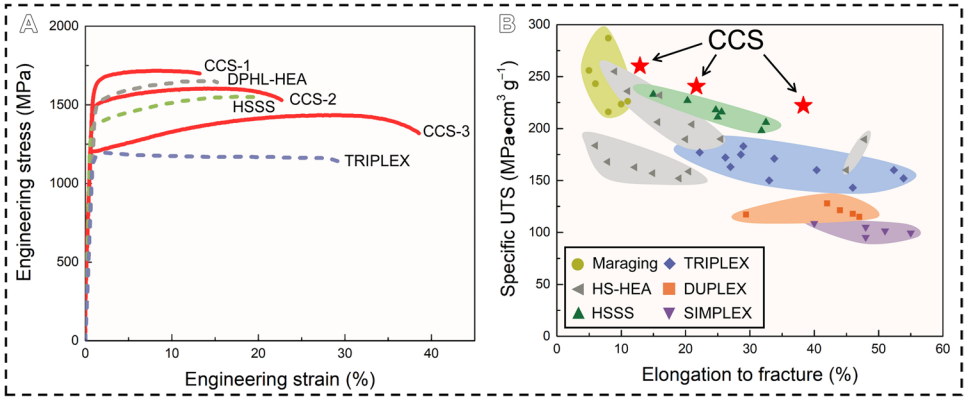

Fig. 3. Mechanical properties of CCSs. (**A**) Engineering stress-strain curves of CCSs. CCS-1, CCS-2, and CCS-3 correspond to CCSs annealed at 800°, 850°, and 900°C, respectively. Tensile properties of the CCSs together with those of representative conventional lightweight steels (TRIPLEX) (*36*), HSSS (*6*), and high-strength dual-phase heterogeneous lamella structured HEAs (DPHL-HEAs) (*21*) are shown for comparison. As representative examples of advanced lightweight steels and high-strength HEAs, the HSSS and DPHL chosen here have similar grain sizes compared to our CCSs. (**B**) Plot of specific UTS (UTS per mass density) as a function of elongation for CCSs and the reference alloys named above. The overall mechanical performance of our CCSs surpasses that of any other high-strength HEAs (HS-HEA) (*21*, *24*–*33*), conventional lightweight steels [including SIMPLEX (*35*), DUPLEX (*34*, *36*), and TRIPLEX (*4*, *36*)], advanced lightweight steels (HSSS) (*6*, *7*), and high-strength maraging steels (*22*, *23*).

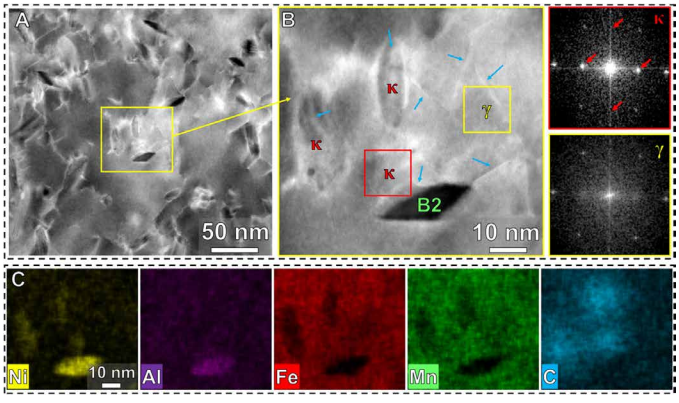

Fig. 4. Deformation microstructures of the CCS at 1.5% strain. (**A**) LAADF-STEM image showing the dislocations (in bright contrast) in the deformed CCS-1. (**B**) Zoom-in image of the marked region in (A). Dislocations are highlighted by the blue arrows. Austenitic (γ) matrix and κ-carbide are identified by FFT patterns, and the B2 phase is detected by EDS maps in (**C**). Dislocations cut through γ matrix and κ-carbide, whereas the bypassing mechanism is shown for the B2 phase.

interrupted by the incoherent B2 precipitates already at a nanoscopic scale before it can get critical. The dense backpack arrangement between the two types of particles does not allow percolative dislocation flow through shearable material; i.e., the topology also plays an important role in this concept. The piling up of dislocations around the B2 particles leads to large long-range back stresses, an effect that further contributes to strain hardening (*7*). This stabilizes plastic deformation and accounts for the alloy's high ductility as well.

In summary, we developed a new class of CCSs with an excellent combination of low mass density (6.6 g/cm^3), very high specific tensile strength (up to 260 MPa·cm^3 g^{-1}), and good ductility (13 to 38% elongation). This is enabled by a novel concept of complex alloy design that allows us to shift the material's composition into a regime where a dual-nanoprecipitation system is triggered, which consists of a densely stacked backpack topology of shearable κ-carbides and non-shearable B2 particles. This combination leads to a nanoscale homogenization of the plastic flow, providing high strengthening by nanoscale shearing and dislocation bow-out and high formability due to the suppression of strain localization. Also, the CCSs are produced via conventional bulk metallurgical processing, amendable to large-scale industrial production. Our alloy concept thus opens a novel pathway for the development of advanced lightweight materials with superior mechanical properties.

MATERIALS AND METHODS

Materials

The model CCS with a nominal composition Fe-26Mn-16Al-5Ni-5C (at. %) was cast using pure metals and carbon by an induction furnace under Ar atmosphere. The as-cast steels were homogenized at 1200°C for 1 hour and quenched in water, followed by hot-rolling at 1100°C to a thickness of 2.5 mm and, further, by cold-rolling to a thickness of 1 mm. The resulting steels were annealed for 3 min at 800°, 850°, and 900°C by using a DIL805A/D dilatometer. The heat treatments were carried out in vacuum conditions, with a heating rate of 50°C/s and a cooling rate of 220°C/s. The chemical compositions of the steel were measured by wet-chemical analysis, as shown in the Supplementary Materials and table S1.

Microstructural characterization

XRD measurements were conducted using an x-ray diffractometer (ISO-DEBYEFLEX 3003) with Co K_α (wavelength of 1.788965 Å). EBSD measurements were performed on a Zeiss-CrossBeam XB 1540 FIB (focused ion beam) SEM (scanning electron microscope) operated at 15 kV. BSE imaging was examined by a Zeiss-Merlin SEM operated at 30 kV.

We further performed TEM characterization following procedures described in our previous report (*39*). DF TEM, BF TEM, and SAED were carried out by an image aberration–corrected FEI Titan Themis at 300 kV. EDS and LAADF and HAADF STEM were conducted by using a probe aberration–corrected FEI Titan Themis at 300 kV. A probe semi-convergence angle of 17 mrad and inner and outer semi-collection angles ranging from 73 to 350 mrad were

used for the HAADF-STEM mode. A probe semi-convergence angle of 17 mrad and inner and outer semi-collection angles from 14 to 63 mrad were operated for the LAADF-STEM mode (*39*).

A local electrode atom probe (CAMECA LEAP 3000 HR and 5000 XR) was used to perform the APT experiments in voltage-pulsing mode with a repetition rate of 200 kHz, a pulse fraction of 15%, and a specimen temperature of −203°C. The APT data were reconstructed and analyzed using IVAS 3.8.4 software (CAMECA Instruments).

Specimens for the SEM characterization were prepared by mechanical polishing, followed by final polishing using a silica oxide suspension. TEM and APT specimens were prepared by a dual FIB-SEM system (FEI Helios NanoLab 600i). Thin foils with a thickness of ~100 μm were prepared for the examination of deformation microstructures. Specimens were electropolished in an electrolyte of 30% nitric acid in methanol using a Struers TenuPol-5 at a voltage of ~10 V and a temperature of −30°C.

Mechanical testing

Dog-bone specimens with a gauge length of 4 mm, a width of 2 mm, and a thickness of 1 mm were used for tensile tests. Tensile tests were performed at room temperature with an initial strain rate of 1×10^{-3} s^{-1} using a Kammrath & Weiss tensile stage. Aramis system (GOM GmbH) was used to measure the local strain evolution during tensile testing based on a digital image correlation method.

Precipitation

EBSD phase maps revealed the existence of B2 particles at both hot-rolling and final states (after thermal-mechanical treatments), with similar volume fractions, as shown in Fig. 1B and fig. S6A. We can hardly find B2 phase under the homogenization state (before hot-rolling; see fig. S7). Thus, the B2 particles with relatively larger sizes (100 to 1000 nm) detected by EBSD (~1 vol. %) were formed during hot-rolling. Extremely fine precipitates of B2 and κ-carbide with very high number density captured by TEM and APT (Fig. 2) were formed during the annealing. The size distribution of these very fine precipitates was evaluated from APT atomic maps, as displayed in the Supplementary Materials and figs. S3 (C and D). The average size of these fine B2 precipitates is ~6 nm, which is much smaller than that in the previously reported HSSS (50 to 300 nm) (*6*). EBSD analysis results of our model CCSs annealed at higher temperatures, i.e., 850° and 900°C, are shown in the Supplementary Materials, figs. S8 and S9, respectively. As the annealing temperature increases from 800° to 900°C, the fraction of recrystallized area increases from 8 to 57%, and the average grain size increases from 0.35 to 1.5 μm. Also, the accompanying coarsening of precipitates due to the higher annealing temperature further leads to the increase of the average spacing among the precipitates from dozens of nanometers to hundreds of nanometers (see figs. S3A and S9D). It is worth noting that grain boundaries act neither as preferred sites for precipitates nor as regions where larger precipitates are formed compared to the grain interiors. This means that the finely dispersed precipitates show nearly homogeneous distribution over all grain boundaries and grain interior regions (see fig. S9D).

Strengthening mechanisms

Multiple strengthening mechanisms contribute to the high strength of CCSs. To evaluate the specific contributions of each mechanism, the yield strength (σ_y) of the current CCSs can be given by

$$\sigma_y = \sigma_0 + \sigma_{gr} + \sigma_{ds} + \sigma_p \quad (1)$$

where σ_0 is the lattice friction stress, σ_{gr} is the stress arising from the grain boundaries strengthening, σ_{ds} is the stress resulting from the dislocation strengthening, and σ_p is the stress from the precipitate strengthening.

The grain boundary strengthening follows the Hall-Petch relationship, which can be calculated by (*40*)

$$\sigma_{gr} = f_{RX} \cdot k/\sqrt{d_{RX}} \quad (2)$$

where f_{RX} refers to the volume fraction of the recrystallized region, k is the value of Hall-Petch slope [14.55 MPa·$mm^{1/2}$ (*41*)], and d_{RX} is the grain size of the recrystallized region (~350 nm). The contribution from the grain boundaries (σ_{gr}) is around 62 MPa. The strengthening from the dislocation is given by the Taylor hardening law (*40*)

$$\sigma_{ds} = f_{NRX} M \alpha G b \sqrt{\rho_{ds}} \quad (3)$$

where f_{NRX} refers to the volume fraction of the non-recrystallized region, M is the Taylor factor of FCC alloys (3.06), α is a constant (0.2), G is the shear modulus, b is the magnitude of the Burgers vector (0.26 nm), and ρ_{ds} is the dislocation density. The shear modulus was obtained by the equation $G = E/2(1 + \nu)$, where E is the Young's modulus and ν is Poisson's ratio (ν = 0.25 for austenite steels). The values of Young's modulus of lightweight steels (with 25 to 30 wt. % Mn and 8 to 10 wt. % Al) mostly range from 160 to 180 GPa, although the compositions varied (*2*). Correspondingly, the values of shear modulus are in the range of 64 to 72 GPa. We thus took the average value, i.e., 68 GPa, for the shear modulus. In the present study, the dislocation strengthening effect mainly results from the geometrically necessary dislocations (GNDs) as the densities of retained statistically stored dislocations were very low due to the recovery upon annealing (*42*). The density of GNDs can be calculated by the following expression (*43*)

$$\rho_{ds} = 2\theta/\mu b \quad (4)$$

where θ is the misorientation angle and μ is the unit length [$\mu = 10^{-5}$ m (*43*)]. The misorientation angle was estimated on the basis of the kernel average misorientation maps from EBSD analysis, which gives the dislocation density of 1.74×10^{13} m^{-2}. Thus, the strengthening provided by dislocations (σ_{ds}) is 42 MPa. Since the strengthening effect from lattice friction, grain boundaries, and dislocations is known, the strengthening arising from the dual-nanoprecipitation can be calculated by

$$\sigma_p = \sigma_y - \sigma_0 - \sigma_{gr} - \sigma_{ds} \quad (5)$$

To accurately evaluate the lattice friction stress of the FCC matrix, we performed additional tensile tests to measure the yield strength of a homogenized alloy without Ni (Fe-26Mn-16Al-5C, at. %), a composition very close to that of the FCC matrix in our CCS. This gave a yield strength value of 445 MPa. The homogenized alloy had an austenite structure with a very large average grain size of ~92 μm. The lattice friction stress was then obtained by subtracting the grain boundary strengthening from the measured yield strength, which gave a value of 397 MPa. Thus, the nanoprecipitate strengthening contribution (σ_p) is calculated as 1082 MPa.

This shows that the dual-nanoprecipitate strengthening mechanism plays a larger role in the yield strength than all other strengthening mechanisms.

Specific UTS

The specific UTS is defined as the ratio between the UTS and the alloy's mass density. The densities of steels and alloys (ρ) are estimated on the basis of the regression formula (*44*)

$$1/\rho = \sum_i \frac{1}{\rho_i} C_i^{wt}(s) \quad (6)$$

where ρ_i is the density of element i and $C_i^{wt}(s)$ is the mass content of element i.

The concept of CCSs

Conventional lightweight steels usually contain less than three major elements (e.g., Fe, Mn, and Al each has a concentration of no less than 5 at. %), and carbon contents are typically lower than 4 at. % (*2*). The advanced lightweight steels (HSSS) (*6*) involve the addition of Ni in the Fe-Mn-Al-C lightweight steel, while Fe content is still higher than 60 at. %, and the contents of additional elements are very low (e.g., C <5 at. %). We redesigned the lightweight steels by making use of the CCA or HEA concept, which is referred to as CCS (e.g., Fe-26Mn-16Al-5Ni-5C, at. %) in the present study. Our CCS consists of five major elements where the content of each element is around or above 5 at. %, which belongs to realms of CCAs/HEAs based on the definition (*45*). In this work, the novel concept of CCS allows us to use the merits from multi–principal elements here of Fe, Mn, Al, Ni, and C. The basic roles of each of these elements and in part also their solubility limits were described in the literature (*2*, *12*–*14*). Thus, the unique dual-nanoprecipitation of κ-carbide and B2 forms, which is previously unreachable. This further gives rise to outstanding mechanical properties that outcompete those of existing lightweight steels.

SUPPLEMENTARY MATERIALS

Supplementary material for this article is available at http://advances.sciencemag.org/cgi/content/full/6/46/eaba9543/DC1

REFERENCES AND NOTES

1. M. Militzer, A synchrotron look at steel. *Science* **298**, 975–976 (2002).
2. S. Chen, R. Rana, A. Haldar, R. K. Ray, Current state of Fe-Mn-Al-C low density steels. *Prog. Mater. Sci.* **89**, 345–391 (2017).
3. D. Raabe, C. C. Tasan, H. Springer, M. Bausch, From high-entropy alloys to high-entropy steels. *Steel Res. Int.* **86**, 1127–1138 (2015).
4. G. Frommeyer, U. Brüx, Microstructures and mechanical properties of high-strength Fe-Mn-Al-C light-weight TRIPLEX steels. *Steel Res. Int.* **77**, 627–633 (2006).
5. E. Hornbogen, K.-H. Zum Gahr, Distribution of plastic strain in alloys containing small particles. *Metallography* **8**, 181–202 (1975).
6. S. H. Kim, H. Kim, N. J. Kim, Brittle intermetallic compound makes ultrastrong low-density steel with large ductility. *Nature* **518**, 77–79 (2015).
7. M. X. Yang, F. P. Yuan, Q. G. Xie, Y. D. Wang, E. Ma, X. L. Wu, Strain hardening in Fe–16Mn–10Al–0.86C–5Ni high specific strength steel. *Acta Mater.* **109**, 213–222 (2016).
8. I. Baker, M. Wu, Z. Wang, Eutectic/eutectoid multi-principle component alloys: A review. *Mater. Charact.* **147**, 545–557 (2019).
9. J. W. Yeh, S. K. Chen, S. J. Lin, J. Y. Gan, T. S. Chin, T. T. Shun, C. H. Tsau, S. Y. Chang, Nanostructured high-entropy alloys with multiple principal elements: Novel alloy design concepts and outcomes. *Adv. Eng. Mater.* **6**, 299–303 (2004).
10. Z. Li, K. G. Pradeep, Y. Deng, D. Raabe, C. C. Tasan, Metastable high-entropy dual-phase alloys overcome the strength-ductility trade-off. *Nature* **534**, 227–230 (2016).
11. B. Gludovatz, A. Hohenwarter, D. Catoor, E. H. Chang, E. P. George, R. O. Ritchie, A fracture-resistant high-entropy alloy for cryogenic applications. *Science* **345**, 1153–1158 (2014).
12. R. L. Klueh, P. J. Maziasz, E. H. Lee, Manganese as an austenite stabilizer in Fe-Cr-Mn-C steels. *Mater. Sci. Eng. A* **102**, 115–124 (1988).
13. H. Huang, D. Gan, P. W. Kao, Effect of alloying additions on the κ phase precipitation in austenitic Fe-Mn-Al-C alloys. *Scr. Metall. Mater.* **30**, 499–504 (1994).
14. J. Breuer, A. Grün, F. Sommer, E. J. Mittemeijer, Enthalpy of formation of B2-$Fe_{1-x}Al_x$ and B2-$(Ni,Fe)_{1-x}Al_x$. *Metall. Mater. Trans. B Process Metall. Mater. Process. Sci.* **32**, 913–918 (2001).
15. R. D. Noebe, R. R. Bowman, M. V. Nathal, Physical and mechanical properties of the B2 compound NiAl. *Int. Mater. Rev.* **38**, 193–232 (1993).
16. D. Raabe, H. Springer, I. Gutierrez-Urrutia, F. Roters, M. Bausch, J. B. Seol, M. Koyama, P. P. Choi, K. Tsuzaki, Alloy design, combinatorial synthesis, and microstructure–property relations for low-density Fe-Mn-Al-C austenitic steels. *JOM* **66**, 1845–1856 (2014).
17. K. H. Han, J. C. Yoon, W. K. Choo, TEM evidence of modulated structure in Fe-Mn-Al-C austenitic alloys. *Scr. Metall.* **20**, 33–36 (1986).
18. W. K. Choo, J. H. Kim, J. C. Yoon, Microstructural change in austenitic Fe-30.0wt%Mn-7.8wt%Al-1.3wt%C initiated by spinodal decomposition and its influence on mechanical properties. *Acta Mater.* **45**, 4877–4885 (1997).
19. M. C. Li, H. Chang, P. W. Kao, D. Gan, The effect of Mn and Al contents on the solvus of κ phase in austenitic Fe-Mn-Al-C alloys. *Mater. Chem. Phys.* **59**, 96–99 (1999).
20. H. Zhao, Y. Chen, B. Gault, S. K. Makineni, D. Ponge, D. Raabe, (Al, Zn)$_3$Zr dispersoids assisted η′ precipitation in anAl-Zn-Mg-Cu-Zr alloy. *Materialia* **10**, 100641 (2020).
21. P. Shi, W. Ren, T. Zheng, Z. Ren, X. Hou, J. Peng, P. Hu, Y. Gao, Y. Zhong, P. K. Liaw, Enhanced strength-ductility synergy in ultrafine-grained eutectic high-entropy alloys by inheriting microstructural lamellae. *Nat. Commun.* **10**, 489 (2019).
22. W. Sha, H. Leitner, Z. Guo, W. Xu, Phase transformations in maraging steels, in *Phase Transformations in Steels*, E. Pereloma, D. V. Edmonds, Eds. (Woodhead, 2012), vol. 2, chap. 11.
23. S. Jiang, H. Wang, Y. Wu, X. Liu, H. Chen, M. Yao, B. Gault, D. Ponge, D. Raabe, A. Hirata, M. Chen, Y. Wang, Z. Lu, Ultrastrong steel via minimal lattice misfit and high-density nanoprecipitation. *Nature* **544**, 460–464 (2017).
24. Y. Dong, X. Gao, Y. Lu, T. Wang, T. Li, A multi-component $AlCrFe_2Ni_2$ alloy with excellent mechanical properties. *Mater. Lett.* **169**, 62–64 (2016).
25. M. Komarasamy, T. Wang, K. Liu, L. Reza-Nieto, R. S. Mishra, Hierarchical multi-phase microstructural architecture for exceptional strength-ductility combination in a complex concentrated alloy via high-temperature severe plastic deformation. *Scr. Mater.* **162**, 38–43 (2019).
26. Y. J. Liang, L. Wang, Y. Wen, B. Cheng, Q. Wu, T. Cao, Q. Xiao, Y. Xue, G. Sha, Y. Wang, Y. Ren, X. Li, L. Wang, F. Wang, H. Cai, High-content ductile coherent nanoprecipitates achieve ultrastrong high-entropy alloys. *Nat. Commun.* **9**, 4063 (2018).
27. Y. Lu, X. Gao, L. Jiang, Z. Chen, T. Wang, J. Jie, H. Kang, Y. Zhang, S. Guo, H. Ruan, Y. Zhao, Z. Cao, T. Li, Directly cast bulk eutectic and near-eutectic high entropy alloys with balanced strength and ductility in a wide temperature range. *Acta Mater.* **124**, 143–150 (2017).
28. K. Ming, X. Bi, J. Wang, Precipitation strengthening of ductile $Cr_{15}Fe_{20}Co_{35}Ni_{i20}Mo_{10}$ alloys. *Scr. Mater.* **137**, 88–93 (2017).
29. K. Ming, X. Bi, J. Wang, Strength and ductility of CrFeCoNiMo alloy with hierarchical microstructures. *Int. J. Plast.* **113**, 255–268 (2019).
30. C.-W. Tsai, M.-H. Tsai, J.-W. Yeh, C.-C. Yang, Effect of temperature on mechanical properties of $Al_{0.5}CoCrCuFeNi$ wrought alloy. *J. Alloys Compd.* **490**, 160–165 (2010).
31. Q. Wang, Y. Ma, B. Jiang, X. Li, Y. Shi, C. Dong, P. K. Liaw, A cuboidal B2 nanoprecipitation-enhanced body-centered-cubic alloy $Al_{0.7}CoCrFe_2Ni$ with prominent tensile properties. *Scr. Mater.* **120**, 85–89 (2016).
32. T. Yang, Y. L. Zhao, Y. Tong, Z. B. Jiao, J. Wei, J. X. Cai, X. D. Han, D. Chen, A. Hu, J. J. Kai, K. Lu, Y. Liu, C. T. Liu, Multicomponent intermetallic nanoparticles and superb mechanical behaviors of complex alloys. *Science* **362**, 933–937 (2018).
33. Y. L. Zhao, T. Yang, Y. Tong, J. Wang, J. H. Luan, Z. B. Jiao, D. Chen, Y. Yang, A. Hu, C. T. Liu, J. J. Kai, Heterogeneous precipitation behavior and stacking-fault-mediated deformation in a CoCrNi-based medium-entropy alloy. *Acta Mater.* **138**, 72–82 (2017).
34. S. W. Hwang, J. H. Ji, E. G. Lee, K.-T. Park, Tensile deformation of a duplex Fe–20Mn–9Al–0.6C steel having the reduced specific weight. *Mater. Sci. Eng. A* **528**, 5196–5203 (2011).
35. H. Springer, D. Raabe, Rapid alloy prototyping: Compositional and thermo-mechanical high throughput bulk combinatorial design of structural materials based on the example of 30Mn–1.2C–xAl triplex steels. *Acta Mater.* **60**, 4950–4959 (2012).
36. Y. Sutou, N. Kamiya, R. Umino, I. Ohnuma, K. Ishida, High-strength Fe-20Mn-Al-C-based alloys with low density. *ISIJ Int.* **50**, 893–899 (2010).
37. M. J. Yao, E. Welsch, D. Ponge, S. M. H. Haghighat, S. Sandlöbes, P. Choi, M. Herbig, I. Bleskov, T. Hickel, M. Lipinska-Chwalek, P. Shanthraj, C. Scheu, S. Zaefferer, B. Gault, D. Raabe, Strengthening and strain hardening mechanisms in a precipitation-hardened high-Mn lightweight steel. *Acta Mater.* **140**, 258–273 (2017).
38. Y. Liao, I. Baker, On the room-temperature deformation mechanisms of lamellar-structured $Fe_{30}Ni_{20}Mn_{35}Al_{15}$. *Mater. Sci. Eng. A* **528**, 3998–4008 (2011).

39. W. Lu, C. H. Liebscher, F. Yan, X. Fang, L. Li, J. Li, W. Guo, G. Dehm, D. Raabe, Z. Li, Interfacial nanophases stabilize nanotwins in high-entropy alloys. *Acta Mater.* **185**, 218–232 (2020).
40. T. H. Courtney, *Mechanical Behavior of Materials* (Waveland Press, 2005).
41. M.-Y. Seok, I.-C. Choi, J. Moon, S. Kim, U. Ramamurty, J.-i. Jang, Estimation of the Hall–Petch strengthening coefficient of steels through nanoindentation. *Scr. Mater.* **87**, 49–52 (2014).
42. J. Su, D. Raabe, Z. Li, Hierarchical microstructure design to tune the mechanical behavior of an interstitial TRIP-TWIP high-entropy alloy. *Acta Mater.* **163**, 40–54 (2019).
43. D. Jorge-Badiola, A. Iza-Mendia, I. Gutiérrez, Study by EBSD of the development of the substructure in a hot deformed 304 stainless steel. *Mater. Sci. Eng. A* **394**, 445–454 (2005).
44. U. Bohnenkamp, R. Sandström, Evaluation of the density of steels. *Steel Res.* **71**, 88–93 (2000).
45. Z. P. Lu, H. Wang, M. W. Chen, I. Baker, J. W. Yeh, C. T. Liu, T. G. Nieh, An assessment on the future development of high-entropy alloys: Summary from a recent workshop. *Intermetallics* **66**, 67–76 (2015).

Acknowledgments: The contributions of H. Springer, D. Klapproth, F. Rütters, M. Nellessen, and M. Adamek are acknowledged. **Funding:** Z.W. was supported by the Alexander von Humboldt Stiftung. Z.L. would like to acknowledge the financial support from the National Natural Science Foundation of China (grant no. 51971248). **Author contributions:** Z.W., D.R., and Z.L. conceived the project. Z.W. and Z.L. designed the alloy. Z.W. conducted the SEM/EBSD characterization and mechanical tests. W.L. conducted the TEM/STEM characterization. Z.W., H.Z., and J.H. conducted the APT characterization. C.H.L. and D.P. contributed to the data analysis. Z.W., D.R., and Z.L. wrote the manuscript. All authors contributed to the discussion of the results and commented on the manuscript. **Competing interests:** The authors declare that they have no competing interests. **Data and materials availability:** All data needed to evaluate the conclusions in the paper are present in the paper and/or the Supplementary Materials. Additional data related to this paper may be requested from the corresponding authors.

Submitted 18 January 2020
Accepted 29 September 2020
Published 13 November 2020
10.1126/sciadv.aba9543

Citation: Z. Wang, W. Lu, H. Zhao, C. H. Liebscher, J. He, D. Ponge, D. Raabe, Z. Li, Ultrastrong lightweight compositionally complex steels via dual-nanoprecipitation. *Sci. Adv.* **6**, eaba9543 (2020).

ScienceAdvances

Ultrastrong lightweight compositionally complex steels via dual-nanoprecipitation

Zhangwei WangWenjun LuHuan ZhaoChristian H. LiebscherJunyang HeDirk PongeDierk RaabeZhiming Li

Sci. Adv., 6 (46), eaba9543. • DOI: 10.1126/sciadv.aba9543

Science Advances (ISSN 2375-2548) is published by the American Association for the Advancement of Science. 1200 New York Avenue NW, Washington, DC 20005. The title *Science Advances* is a registered trademark of AAAS.